Comparison of an Enhanced Distorted Born Iterative Method and the Multiplicative-Regularized Contrast Source Inversion method

Colin Gilmore, *Student Member, IEEE*, Puyan Mojabi, and Joe LoVetri, *Senior Member, IEEE*

***Abstract*—For 2D transverse magnetic (TM) microwave inversion, multiplicative-regularized contrast source inversion (MR-CSI), and the distorted Born iterative method (DBIM) are compared. The comparison is based on a computational resource analysis, inversion of synthetic data, and inversion of experimentally collected data from both the Fresnel and UPC Barcelona data sets. All inversion results are blind, but appropriate physical values for the reconstructed contrast are maintained. The data sets used to test the algorithms vary widely in terms of the background media, antennas, and far/near field considerations. To ensure that the comparison is replicable, an automatic regularization parameter selection method is used for the additive regularization within the DBIM, which utilizes a fast implementation of the L-curve method and the Laplacian regularizer. While not used in the classical DBIM, we introduce an MR term to the DBIM in order to provide comparable results to MR-CSI. The introduction of this MR term requires only slight modifications to the classical DBIM algorithm, and adds little computational complexity. The results show that with the addition of the MR term in the DBIM, the two algorithms provide very similar inversion results, but with the MR-CSI method providing advantages for both computational resources and ease of implementation.**

***Index Terms*—Biomedical electromagnetic imaging, electromagnetic scattering inverse problems, inverse problems.**

I. Introduction

THE microwave inverse scattering problem has been of interest for many years and research into this field has led to the development of many inversion algorithms. The ability to exploit previously unutilized tissue contrast mechanisms, as well as the ability to perform quantitative imaging of the complex permittivity, make microwave imaging a strong contender to complement other biomedical imaging modalities. Significant progress in microwave imaging has been accomplished in the last decade, with experimental prototypes having been used for the imaging of excised pigs legs [1], a canine heart, [2], and breast cancer [3].

The greatest challenge in using microwaves for imaging purposes is the fact that direct-ray models and other linear scattering models, used in most other imaging modalities, do not sufficiently approximate the actual physics. Essentially, at the wavelengths of the microwave radiation being used, the electromagnetic waves scatter multiple times, refract through and diffract around the object of interest, and generally do not follow simple paths within the imaging region. Research on biomedical microwave imaging that has made use of linearizing assumptions about the wave-propagation within the breast, e.g., [4]–[7], shows that using direct-ray and linear scattering models that ignore higher order effects, while providing some useful qualitative images, cannot quantitatively reconstruct the bulk-electrical parameters. Thus, accurate quantitative microwave imaging (MWI) requires the use of the full nonlinear inverse problem formulation, which is an ill-posed mathematical problem. Such problems are notoriously difficult to solve because of the nonuniqueness and lack of stability of the solution: more than one solution exists to the formulated mathematical problem and a small change in the data may result in a drastically different solution [8]. Thus, some regularization technique (i.e., selecting one of the infinite number of possible solutions) is required to come up with the correct (or approximate) physical solution. Many of these techniques require that a regularization parameter be chosen and the final solution and computational effort can be very sensitive to the value of this regularization parameter.

In recent years, techniques have been developed to solve the full nonlinear inverse problem and these techniques have been used to give successful quantitative reconstructions of biological materials from experimentally collected data at limited (even single) frequencies. These inversion techniques offer a quantitative reconstruction of the contrast but are mathematically more complicated than the linearized techniques, and usually take more computational resources to solve. Broadly speaking, there are two different approaches that have been successfully used to solve the inverse scattering problem [9]. The two approaches are distinguished by their use (or lack of use) of a forward solver, as well as the selection of the objective function that is minimized. The first approach, known as the conventional type, formulates the objective function based solely on the scattered data outside the object of interest (OI) and uses repeated calls to a forward solver during the iterative minimization. Methods falling under the conventional class include the distorted Born iterative method (DBIM) [10], Modified Newton type minimizations [3], [9], and global optimization techniques, e.g., genetic algorithms [11]. The second class of approaches, which are distinguished by the absence of a forward solver and

Manuscript received May 28, 2008; revised January 15, 2009. First published June 05, 2009; current version published August 05, 2009.

The authors are with the Department of Electrical and Computer Engineering, University of Manitoba, Winnipeg, Canada (e-mail: cgilmore@ee.umanitoba.ca; pmojabi@ee.umanitoba.ca; lovetri@ee.umanitoba.ca).

Color versions of one or more of the figures in this paper are available online at http://ieeexplore.ieee.org.

Digital Object Identifier 10.1109/TAP.2009.2024478

the use of an objective function based on both scattered fields outside the OI and total fields inside the OI, is known as the modified gradient type. Examples of these inversion techniques include the modified gradient method (MGM) [12] and the contrast source inversion (CSI) method [13], [14].

In this paper we consider and compare an example of each of these two types of inversion techniques, working blindly with a wide range of scattering data collected from multiple imaging systems. The modified gradient type is represented by the multiplicative regularized-contrast source inversion (MR-CSI) method [13], [14] and the conventional type by the DBIM [10]. Both are applied to the 2D transverse magnetic (TM) inverse problem. While both conventional and modified gradient types of inversion algorithms have provided successful microwave imaging results, the relative performance of these two groups of algorithms, in terms of inversion quality, regularization needs, and computational resources, has not been investigated. Although it is clear that the absence of a forward solver makes each iteration of the modified gradient type method significantly more efficient at each iteration, the exact computational burden comparison has not, to the best of our knowledge, been completed. In addition, many more iterations are needed in order to obtain convergence using modified gradient type inversion.

Of key importance is that for the basic data misfit cost-functional, associated with the inverse problem, some type of regularization is required, as the solution of this functional is ill-posed. In the (non-MR) CSI method, this regularization is provided by adding a second term to the data misfit functional, based on the domain/object equation, which effectively regularizes the inverse problem in many cases, e.g., [13] (this is sometimes called the Maxwell regularizer [15]). Additional regularization and improved inversion results may be achieved with the use of an MR term [16]. For both the Maxwell and multiplicative regularizers, the (MR) CSI algorithm automatically selects the regularization parameters.

For the conventional type algorithms, e.g., DBIM, which only use the data misfit cost-functional, there is a choice as to when the regularization is applied. The data misfit cost-functional may be regularized before the optimization process [9], [17], or the cost-functional may be regularized at each step of the optimization process (once the problem has been linearized) [3], [10]. In this paper, we consider the second type of conventional algorithm which regularizes the problem after linearization (as in DBIM).

Generally, for DBIM, Tikhonov regularization has been used, which requires the choice of a regularization parameter. The regularization parameter is typically selected via considerable numerical experimentation, or knowledge of the noise level in the measured data (i.e., the discrepancy principle [18]). The lack of a consistently used method in the selection of a regularization parameter for DBIM clouds the direct comparison between these two classes of inversion algorithm. It also makes blind inversion, defined as inversion of microwave scattering data without any prior knowledge, difficult with the DBIM algorithm. In addition, the significant time and effort needed to determine the regularization parameter is left out of published computational times, which again makes a direct comparison problematic.

However, recent advances in regularization parameter choice methods have made it possible to compare these types of algorithms and their performance in blind inversion problems. In this work, we make use of an automatic parameter choice method [19] where the regularization parameter in DBIM is automatically set to the optimal value (in the sense of the L-curve method [20]) at each iteration of the inversion process, without user input or advance knowledge of the noise level, system configuration, or other information about the scatterer. The use of such an automatic parameter choice method for DBIM makes the results reproducible and allows for a fair comparison between these two techniques.

In addition, motivated by the success of multiplicative regularization (MR) in the CSI method, and the desire to make a fair comparison between the MR-CSI and DBIM techniques, in this paper we modify the DBIM with an MR term. This modified DBIM still requires additive regularization at each iteration and we utilize the MR term after the Tikhonov regularization has been applied. The MR term enhances the inversion results due to its edge-preserving properties.

The paper is organized as follows. Section II discusses the basic formulation of the inverse problem, Section III presents the MR-CSI method and Section IV presents the DBIM and our MR modification. In Section V we present a computational cost analysis, as well as the inversion results from synthetic and experimental data. In Section VI we provide conclusions.

II. Formulation of the Problem

We approximate the electromagnetic scattering problem with a 2D TM scalar approximation. We assume inversion targets to be arbitrary inhomogeneous 2D objects in the $x-y$ plane. Consider now an imaging domain $D \subset \mathbb{R}^2$ containing these objects and a measurement surface $S \subset \mathbb{R}^2$ outside of D as depicted in Fig. 1. Let $\mathbf{p}$ and $\mathbf{q}$ denote position vectors in the $x-y$ plane and define the complex electric contrast as

$$\chi(\mathbf{q}) = \frac{\epsilon(\mathbf{q}) - \epsilon_{\mathrm{b}}}{\epsilon_{\mathrm{b}}} \tag{1}$$

where ϵ_b is the complex permittivity of the background medium. The permittivities are taken to be complex so as to allow the modelling of both polarization and conductive losses. With an assumption of an $e^{j\omega t}$ time-dependency, the complex permittivity of an object may be written as

$$\epsilon(\mathbf{q}) = \epsilon'(\mathbf{q}) + j\epsilon''(\mathbf{q}) = \epsilon'(\mathbf{q}) - j\frac{\sigma(\mathbf{q})}{\omega} \tag{2}$$

where σ is the effective conductivity at frequency ω.

For the TM case, the electric field can be represented as $u = \mathbf{E}\cdot\hat{z}$, and the scattered electric field as $u^{\mathrm{s}} = u - u^{\mathrm{inc}}$, where u^{inc} denotes the incident field. All material properties are taken to be nonmagnetic and therefore the permeability is taken as that of free-space, μ_0, throughout the analysis. The wavenumber of the background medium is given by

$$k_{\mathrm{b}} = \sqrt{\omega^2 \mu_0 \epsilon_{\mathrm{b}}}.$$

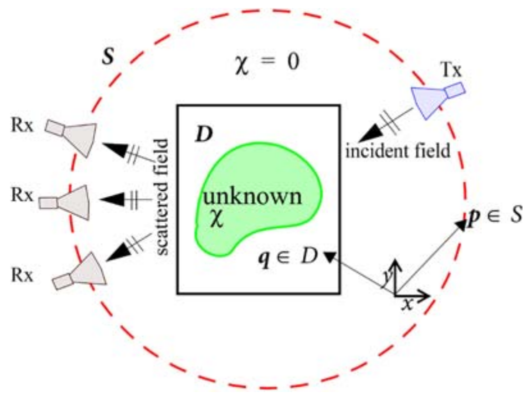

Fig. 1. Basic geometrical model of microwave tomography.

The integral formulation of the so-called *data equation* can be written as

$$u^{\mathrm{s}}(\mathbf{p}) = \mathcal{G}_{\mathrm{S}}\{\chi u\} \qquad \mathbf{p} \in S \tag{3}$$

where the data operator $\mathcal{G}_{\mathrm{S}}\{\cdot\}$ is defined as

$$\mathcal{G}_{\mathrm{S}}\{\psi\} = k_{\mathrm{b}}^2 \int_D G(\mathbf{p},\mathbf{q})\psi(\mathbf{q})d\mathbf{v}(\mathbf{q}) \qquad \mathbf{p} \in S \tag{4}$$

and $G(\mathbf{p},\mathbf{q})$ is the Greens function for the background medium. In the case of a homogeneous background, the Greens function is the standard 2D scalar Greens function

$$G(\mathbf{p},\mathbf{q}) = \frac{1}{4j} H_0^{(2)}\left(k_{\mathrm{b}}|\mathbf{p}-\mathbf{q}|\right) \tag{5}$$

where $H_0^{(2)}(\cdot)$ is the zeroeth order Hankel function of the second kind.

The measurements give us an approximation $\tilde{u}^{\mathrm{s}}(\mathbf{p} \in S)$ for $u^{\mathrm{s}}(\mathbf{p} \in S)$ from which $\chi(\mathbf{q} \in D)$ and $u(\mathbf{q} \in D)$ are to be found. But, given that $\mathcal{G}_{\mathrm{S}}\{\cdot\}$ is a compact integral operator, the data equation is an ill-posed nonlinear integral equation for the unknowns $\chi(\mathbf{q} \in D)$ and $u(\mathbf{q} \in D)$. These two unknowns are also nonlinearly related through the so-called *domain equation*: taking the observation point, $\mathbf{p}$, inside the imaging domain D, the domain equation is written as

$$u^{\mathrm{inc}}(\mathbf{p}) = u(\mathbf{p}) - \mathcal{G}_{\mathrm{D}}\{\chi u\}, \qquad \mathbf{p} \in D \tag{6}$$

where the domain or object operator $\mathcal{G}_{\mathrm{D}}\{\cdot\}$ is defined as

$$\mathcal{G}_{\mathrm{D}}\{\psi\} = k_{\mathrm{b}}^2 \int_D G(\mathbf{p},\mathbf{q})\psi(\mathbf{q})d\mathbf{v}(\mathbf{q}) \qquad \mathbf{p} \in D. \tag{7}$$

Assuming that for each set of measurements, numbered from $m = 1 \cdots T_x$, the object is illuminated by the incident field, u_m^{inc}, the inverse scattering problem can be formulated as the following minimization:

$$\chi = \arg\min_{\chi} \sum_{m=1}^{T_x} \|\tilde{u}_m^{\mathrm{s}} - \mathcal{G}_{\mathrm{S}}\{\chi u_m\}\|_S^2 \text{ subject to :}$$
$$u_m^{\mathrm{inc}}(\mathbf{p} \in D) = u_m(\mathbf{p} \in D) - \mathcal{G}_{\mathrm{D}}\{\chi u_m\} \tag{8}$$

where $\|\cdot\|_S$ denotes the L_2-norm on the measurement surface S.

III. The MR-CSI Method

The MR-CSI algorithm formulates the inverse problem in terms of the contrast, $\chi(\mathbf{p} \in D)$, and contrast sources, $w(\mathbf{p} \in D)$, defined as

$$w_m(\mathbf{p}) = u_m(\mathbf{p})\chi(\mathbf{p}). \tag{9}$$

Using the contrast sources, the domain equation is rewritten

$$\chi(\mathbf{p})u_m^{\mathrm{inc}}(\mathbf{p}) = w_m(\mathbf{p}) - \chi(\mathbf{p})\mathcal{G}_{\mathrm{D}}\{w_m(\mathbf{p})\}. \tag{10}$$

The core of the CSI method is an objective function based on (8), but is written in terms of the contrast and the contrast sources

$$\begin{aligned} F &= F(w_m,\chi) \\ &= \frac{\sum_m \|\tilde{u}_m^{\mathrm{s}} - \mathcal{G}_{\mathrm{S}}\{w_m\}\|_S^2}{\sum_m \|\tilde{u}^{\mathrm{s}}\|_S^2} \\ &\quad + \frac{\sum_m \left\|\chi u_m^{\mathrm{inc}} - w_m + \chi\mathcal{G}_{\mathrm{D}}\{w_m\}\right\|_D^2}{\sum_m \|\chi u_m^{\mathrm{inc}}\|_D^2} \end{aligned} \tag{11}$$

where $\|\cdot\|_D$ denotes the L_2-norm on D. The normalization terms in the denominators are used to balance between the data and domain equation errors.

In the CSI method, the objective function, (11), is minimized via the formation of two interlaced sequences of the unknowns: a sequence of estimates of the contrast, $\{\chi_n\}$ which is interlaced with a sequence of estimates of the contrast sources $\{w_{m,n}\}$ where n represents the iteration number. For every step of the CSI method, each sequence is updated via the a single step of the CG minimization algorithm while assuming that the other unknown is a constant. The iterative process is continued until a desired minimum of the objective function is reached. Details of the CSI method are left to the references (see, e.g., [13], [14]).

While the CSI method alone is sometimes sufficient to successfully invert data [13], the CSI method may be further enhanced through the use of various multiplicative regularizers [14], [21]. It is possible to add these regularizers without the use of an external selection of a regularization parameter. In this work, we utilize a weighted L_2-norm total variation regularizer. The inclusion of this term allows the MR-CSI method to blindly invert complicated data sets (e.g., [14], [22], [23]). With the inclusion of this multiplicative regularizer, the MR-CSI objective function becomes

$$C_n(w_m,\chi) = F_n^{MR}(\chi) \times F(w_m,\chi) \tag{12}$$

The multiplicative regularizer is given as

$$F_n^{MR}(\chi) = \frac{1}{A}\int_D \frac{|\nabla\chi(\mathbf{q})|^2 + \delta_n^2}{|\nabla\chi_{n-1}(\mathbf{q})|^2 + \delta_{n-1}^2} d\mathbf{v}(\mathbf{q}) \tag{13}$$

where A is the area of the imaging region D. The steering parameter δ_{n-1}^2 is chosen to be $F_{n-1}^D \Delta^{-2}$ where F_{n-1}^D is the second term of the CSI objective function, see (11), evaluated at $\chi = \chi_{n-1}$ and Δ is the length of a side of a single cell in the discretized domain. That is, Δ^{-2} represents the reciprocal of the area of a single cell area of the domain D. For example, on a rectangular grid $\Delta^{-2} = 1/(\Delta x \Delta y)$. The minimization of the MR objective function becomes slightly more complicated than the nonregularized case. While the MR term is a constant with respect to the contrast sources, an additional updating step for the contrast is required. The exact details of this step are outlined in [13], [16].

In this paper, operators $\mathcal{G}_{\mathrm{D}}$ and $\mathcal{G}_{\mathrm{S}}$ are evaluated by discretizing the inversion domain with pulse basis functions, utilizing a basic MoM integration, and application of the discretized $\mathcal{G}_{\mathrm{D}}$ operator is accelerated via the FFT [24]. Key in the CSI method is that the operators, $\mathcal{G}_{\mathrm{S}}$ and $\mathcal{G}_{\mathrm{D}}$, do not need to be inverted at each iteration.

IV. Distorted Born Iterative Method

The DBIM, originally proposed by Chew and Wang [10], tries to solve the nonlinear minimization problem given in (8) through an iterative procedure by alternately updating the guesses of the contrast, χ, and the field, u, inside the imaging domain D. Briefly, the DBIM may be summarized as follows.

1) (*Initialization*) Born approximation: assume that the total field in D is the incident field, $u(\mathbf{q}) = u^{\mathrm{inc}}(\mathbf{q})$.
2) (*Initialization*) Solve for the contrast, χ, by minimizing the data (3).
3) Use the new estimate of the contrast as the input to a forward solver and generate a new estimate of the total field, u_n.
4) Check convergence of the algorithm, based on the relative data equation error. That is, if the term
$$F^S = \frac{\sum_m \|\rho_{m,n}\|_S^2}{\sum_m \|\tilde{u}_m^{\mathrm{s}}\|_S^2} \tag{14}$$
is below a set threshold, the algorithm is stopped. Here, the data error is given by $\rho_{m,n} = \tilde{u}_m^{\mathrm{s}} - \mathcal{G}_{\mathrm{S}}\{\chi_n u_{m,n}\}$ where χ_n is the predicted contrast at the nth iteration of the algorithm and $u_{m,n}$ is the total field inside the imaging domain corresponding to mth transmitter in the presence of χ_n.
5) Compute the distorted Greens function operator, written as
$$\mathcal{G}_{\mathrm{S}n}\{\psi\} = \int_{\mathbf{q}\in D} k_{b,n}^2(\mathbf{q}) G_n(\mathbf{p},\mathbf{q})\psi(\mathbf{q}) d\mathbf{v}(\mathbf{q}) \tag{15}$$
where $\mathbf{p} \in S$, $k_{b,n}$ is the wavenumber of the inhomogeneous background with respect to χ_n, and G_n is the distorted Greens function of the inhomogeneous background χ_n. In order to compute G_n we use the forward solver once for each receiver location [10].
6) Utilizing the distorted Greens operator, and the fields from step 3, update the contrast in the form of $\chi_{n+1} = \chi_n + \delta\chi_n$ where $\delta\chi_n$ is obtained by solving the minimization problem:
$$\delta\chi_n = \arg\min_{\delta\chi} \sum_{m=1}^{T_x} \|\rho_{m,n} - \mathcal{G}_{\mathrm{S}n}\{\delta\chi u_{m,n}\}\|_S^2. \tag{16}$$
7) Go back to step 3.

Note that (16) is similar to the initial minimization of the data equation, but is different in the critical respects that it is solving for a relative change in the permittivity and that the operator $\mathcal{G}_{\mathrm{S}n}$ is the distorted operator. To enhance the convergence of DBIM, we employ a line search algorithm similar to [17]: if the error in the data equation due to the correction $\delta\chi_n$ increases, the contrast is updated in the form of $\chi_{n+1} = \chi_n + \upsilon_n\delta\chi_n$ where υ_n is the appropriate step size. The details of the utilized line search algorithm are not presented here but are available in [17].

A. DBIM and Gauss-Newton Optimization

An often utilized microwave imaging method [3], [9] is the Gauss-Newton optimization technique. As was shown in [25], the DBIM is equivalent to the Gauss-Newton technique. Briefly, the Gauss-Newton method [26] seeks the solution to the minimization of the data error
$$\sum_{m=1}^{T_x} \|\rho_m\|_S^2 = \sum_{m=1}^{T_x} \|\tilde{u}_m^{\mathrm{s}} - u_m^{\mathrm{s}}\|_S^2 \tag{17}$$
by approximating the calculated scattered field, u^{s}, with a first order Taylor expansion around the current contrast χ_n,
$$u_m^{\mathrm{s}}(\chi_n + \delta\chi) \approx u_m^{\mathrm{s}}(\chi_n) + J_n\delta\chi \tag{18}$$
where J_n is the Jacobian matrix containing the Fréchet derivative of u_m^{s} with respect to χ evaluated at χ_n. Utilizing this expansion, the Gauss-Newton method seeks the solution
$$\delta\chi_n = \arg\min_{\delta\chi} \sum_{m=1}^{T_x} \|\rho_{m,n} - J_n\delta\chi\|_S^2 \tag{19}$$
which is equivalent to solving the problem $J_n^H J_n \delta\chi = J_n^H \rho_{m,n}$ (which requires regularization). The equivalence of DBIM and the Gauss-Newton optimization method lies in the fact that the Jacobian matrix operating on the update, $J_n\delta\chi$, is equivalent to [27]:
$$J_n\delta\chi \equiv \mathcal{G}_{\mathrm{S}n}\{\delta\chi u_{m,n}\}. \tag{20}$$
With this equivalence, the minimization problem for the Gauss-Newton method (19) is identical to that of the DBIM (16).

B. The DBIM Inverse Solver: Regularization and Regularization Parameter Selection

1) Additive Regularization With Laplacian Regularizer: The linearized inverse problem, (16), while simpler than the full nonlinear inverse problem, is still ill-posed, as the integral operator is continuous and forms a Fredholm integral equation of the first kind [28]. There are some different approaches to stabilize the problem associated with (16). Herein, we use Tikhonov, or additive regularization, [29] which minimizes the cost-functional:
$$\arg\min_{\delta\chi} \left(\sum_{m=1}^{T_x} \|\rho_{m,n} - \mathcal{G}_{\mathrm{S}n}\{\delta\chi u_{m,n}\}\|_S^2 + \lambda^2 \|L\delta\chi\|_D^2 \right) \tag{21}$$
where L is the regularization operator, and λ is the regularization parameter determining the weight of the regularization. In

this paper, we use the Laplacian regularizer, $L = \nabla^2$ (except for a single case, in Fig. 7). With the additive regularization, the null-space of the additive regularizer intersects trivially with the that of the ill-posed operator ensuring a unique solution for the minimization [30]. The value of the regularization parameter λ, which is a real positive number, plays an important role in the overall success of the DBIM. There are different approaches for finding a good regularization parameter in the framework of a Tikhonov functional: for example, the discrepancy principle [18], generalized cross validation (GCV) [31], the L-curve [20], the normalized cumulative periodogram (NCP) [32], [33] and some empirical methods (e.g., [1], [3]).

While all these methods are capable of regularization parameter selection, the discrepancy principle requires knowledge of the noise level in the data, GCV requires that the noise is normally distributed with zero mean, and NCP requires the noise to be additive white noise. However, the L-curve method does not require any information about the noise level, and is generally more robust against different kinds of noise [20]. Herein, the regularization parameter is chosen using a computationally efficient form of the L-curve method which does not need the singular value decomposition (SVD) of the ill-posed matrix. The method is based on the Lanczos bidiagonalization algorithm, and this algorithm iteratively computes the upper and lower bounds of the curvature of the L-curve. The iterations of the algorithm continue until the bounds are guaranteed to be close. In this technique, the matrix operator is only utilized via matrix-vector multiplication making the L-curve method feasible for large-scale inverse problems. This fast L-curve method requires $O(NR_xT_x)$ operations as opposed to the standard L-curve, i.e., using SVD, which requires $O(R_xT_xN^2)$ operations if $R_xT_x \geq N$ or $O(R_x^2T_x^2N)$ when $R_xT_x \leq N$. The details of the algorithm are not presented here, but are available in [19].

As the standard implementation of the fast L-curve method is only valid with the identity regularizer the fast L-curve method requires some modifications. In particular, we need to change the Laplacian form of Tikhonov regularization to the standard identity-form Tikhonov regularization via the solution of an auxiliary equation, $z = R\delta\chi$ where R is the discretized form of the Laplacian operator and z is a dummy variable [30]. The matrix R is a block Toeplitz matrix with Toeplitz blocks (BTTB), and the calculation of $R^{-1}z$ can be done using the CG-FFT algorithm [30]. This extra computational cost is balanced by the superior regularizing properties of the Laplacian operator. After finding an appropriate regularization parameter, (21) can be solved using standard iterative techniques such as the CG method.

2) Multiplicative Regularization: After the DBIM in conjunction with the utilized additive regularization converges to the contrast χ_{AR}, this contrast is further regularized using the multiplicative regularization. Thus, we minimize the multiplicatively regularized cost-functional

$$\chi_{MR} = \arg\min_{\chi} \left(\sum_{m=1}^{T_x} \|\tilde{u}_m^{\mathrm{s}} - \mathcal{G}_{\mathrm{S}}\{\chi u_m\}\|_S^2 \, F_n^{MR}(\chi) \right) \quad (22)$$

where F_n^{MR} is given in (13). This system is minimized via the CG method, and the initial guess is given by χ_{AR}. The field u_m is the total field inside the imaging domain corresponding to the mth transmitter in the presence of χ_{AR}. The gradients are given in [34]. While a general solution of (22) requires many iterations of the CG algorithm, the number of iterations is significantly reduced due to the accurate initial guess of χ_{AR}. Note that this particular regularizer (13) has edge-preserving characteristics [34].

C. Forward Solver

In each iteration of the DBIM, the forward solver is used to find the total electric field inside the imaging domain for a given contrast corresponding to different incident fields and to find the distorted Greens function for the inhomogeneous background. Our forward solver is a method of moments (MoM) solver on a pulse-basis which utilizes the conjugate gradient solution method with matrix multiplication accelerated by the fast Fourier transform [24]. Integrals involved with the MoM are solved using Richmonds method [35].

V. Results

In order to test the blind inversion capabilities of these algorithms, we present inversion results from three different data sets: synthetic data, the Fresnel Institute scattering data, and the UPC Barcelona data set. Each data set has different levels and types of noise, has different background media, and different data collection types (analytic, free-space broad band antennas, and water-submerged narrow band antennas). In all cases presented below, the data were blindly inverted, and all regularization parameters were automatically selected by the algorithm. The only constraints utilized were to keep the permittivity values within physical values (i.e., $Re(\epsilon_r) \geq 1$ and $Im(\epsilon_r) \leq 0$).

Unless otherwise noted, all DBIM reconstructions shown in this section are generated with the Laplacian regularizer and MR.

A. Synthetic Leg Data Results

While the ultimate test of any inversion algorithm must involve experimentally collected scattering data, it is very useful for comparison purposes to have a synthetic data set where the exact, "ideal" contrast is known. Towards this end, we have created a synthetic model of a leg, shown in parts (a) and (b) of Fig. 2. Permittivity values for the model were taken from published values on human tissue [36]. The model consists of a bone (comprised of a marrow core, $\epsilon_r = 5.5 - j0.55$ surrounded by cortical bone, $\epsilon_r = 12.6 - j2.4$), which is inside of a large mass of muscle ($\epsilon_r = 54.8 - j13.0$), surrounded by skin ($\epsilon_r = 39.4 - j12.9$). Data were generated for the model based on a frequency of 1.5 GHz, with 30 transmitters and 30 receivers evenly spaced on a circle of radius 15 cm. The forward solver utilizes a grid of 100 $\times$ 100 cells on a 10 $\times$ 10 cm grid. The inversions are performed on a grid of 100 $\times$ 100 cells on a 10.2 $\times$ 10.2 cm grid (thus avoiding the inverse crime). The "leg" was immersed in a lossless background medium with $\epsilon_r = 77.3$. To every measurement, 3% white noise was artificially added using the formula

$$\tilde{u}_m^{\mathrm{s,Noisy}} = \tilde{u}_m^{\mathrm{s}} + \max\left(|\tilde{u}_m^{\mathrm{s}}|, \forall \tilde{u}_m^{\mathrm{s}}\right) N_s(\alpha + j\beta) \quad (23)$$

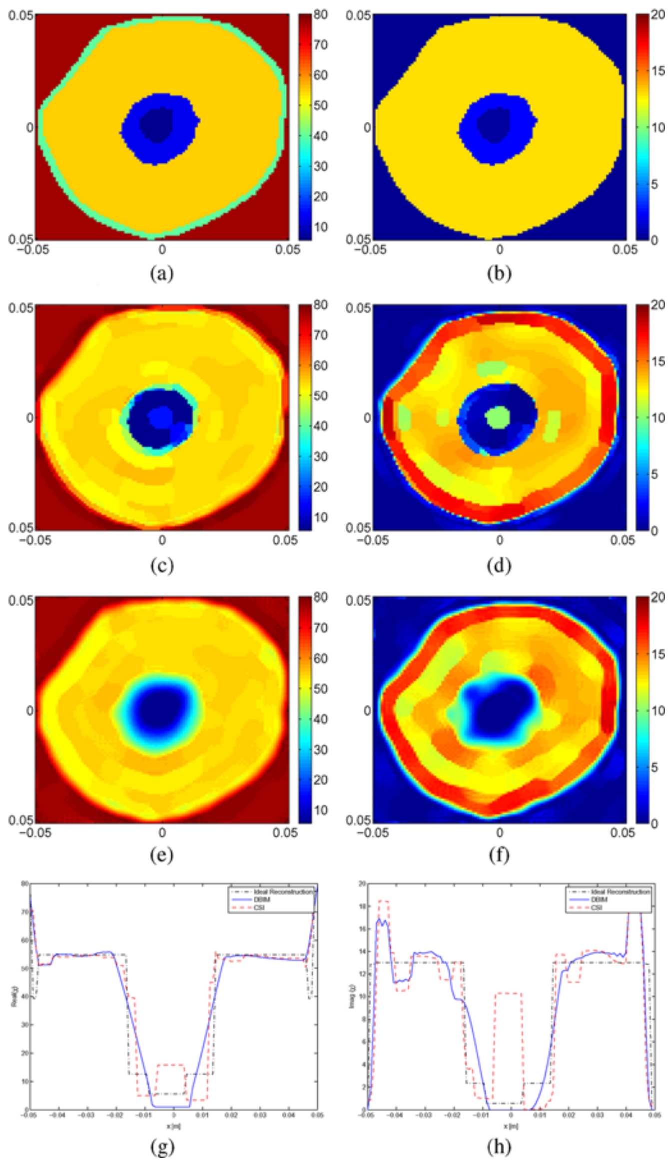

Fig. 2. Synthetic leg data set. (a),(b) the exact permittivities; (c),(d) the MR-CSI reconstruction; (e),(f) the MR-DBIM reconstruction with Laplacian regularizer; (g),(h) a 1D cross section along $y = 0$ of the ideal (black dash-dot line), MR-CSI (red dashed line) and DBIM (blue solid line). The frequency used was $f = 1.5$ GHz.

where $N_s = 0.03$ and α and β are zero-mean random numbers between -1 and 1. The MR-CSI reconstruction is shown in part (b) of Fig. 2, and the DBIM reconstruction is given in part (c). A 1D cross section of the $y = 0$ line for all three plots is shown in part (d). The two reconstructions are remarkably similar, which can be seen particularly clearly in the 2D cross section plots. Neither algorithm accurately resolves the skin, which is not surprising because the skin is approximately 1.5 mm, or $\approx (1/20)\lambda$. The only significant differences between the two results are in the marrow core of the bone, where the CSI algorithm seems to "find" an inhomogeneity associated with the marrow bone, while the DBIM reconstruction provides only a smooth region for the whole bone. However, the permittivity values obtained by the CSI method are not correct, and the DBIM values are closer to the true values.

B. *Fresnel Data Results*

The DBIM and MR-CSI methods were tested on the 2005 Fresnel data set [37]. These data were collected in free-space over a broad frequency range utilizing double-ridged horn antennas, at a distance of 1.67 meters away from the center of the imaging region. Two antennas and a mechanical positioning system are utilized to collect the data. The scatterers are 2D objects elongated enough in the direction so that the objects and fields may be accurately modelled as 2D [37]. To calibrate these data, we utilize the same process as outlined in [23]. Here, we present results from the *FoamTwinDiel* and *FoamMetExt* data sets.

1) FoamTwinDiel: This data set was collected for 18 transmitters, 241 receivers per transmitter, and 9 frequencies from 2–10 GHz in 1 GHz steps. The scatterer, shown in part (a) of Fig. 3, consists of two smaller cylinders of permittivity $\epsilon_r = 3$ where one of the smaller cylinders is embedded in a larger cylinder with $\epsilon_r = 1.45$. As the cylinders are very low loss over the frequency range of interest, we restrict the inversion to $Im(\epsilon_r) = 0$ in this case. When inverting multi-frequency data, we utilize a 'marching-on-frequency' approach for the DBIM method [38]. That is, we invert the data at the lowest frequency, then use the result from that frequency as the first guess for the second frequency (and so on). The MR-CSI utilizes a simultaneous multi-frequency inversion, in that the data from all frequencies is utilized simultaneously. We have implemented a simultaneous multi-frequency inversion for the DBIM, but the marching-on-frequency method provides significantly better results possibly due to the fact that the initial Born approximation used in the DBIM is poor at high frequencies.

Several reconstructions of this object, on a grid of 60×60 cells, are shown in Fig. 3. Part (b) shows the reconstruction at a single frequency of 2 GHz, (c) at a frequency of 6 GHz, and (d) the full data reconstruction from 2–10 GHz. In all cases, the reconstructions are quite similar. Overall, the DBIM overshoots the maximum permittivity of 3 in all three reconstructions, but otherwise the reconstructions are hard to tell apart.

2) FoamMetExt: This data set is collected for 18 transmitters, each with 241 receivers, over seventeen 1 GHz steps in the frequency range of 2–18 GHz. The 2D schematic of the scatterers is shown in Fig. 4(a). In this case, the scatterers consist of a small (radius of 1.55 cm) cylindrical copper rod, next to a weakly scattering dielectric cylinder of radius 4 cm with $\epsilon_r = 1.45$.

The reconstructions on a grid of 60×60, at a frequency of 6 GHz, are shown in Fig. 4. Part (b) shows the MR-CSI method and (c) the DBIM method. Again for this data set, the reconstructions are very similar. In this case, the MR-CSI method gives some oscillations inside the larger scatterer which the DBIM does not. There are some differences inside the copper cylinder, but as there are no fields inside the cylinder (and thus no information about the inside of the scatterer), these differences are not relevant. The full frequency (2–18 GHz) reconstruction is shown in Fig. 5. Part (a) shows the MR-CSI reconstruction, while part (b) shows the DBIM reconstruction. In this case, the two are very similar, with the only significant differences being inside the copper cylinder.

C. *UPC Barcelona Data Set*

The UPC Barcelona data set [39] is a collected from a near-field single frequency scanner, pictured in [40]. There are 64

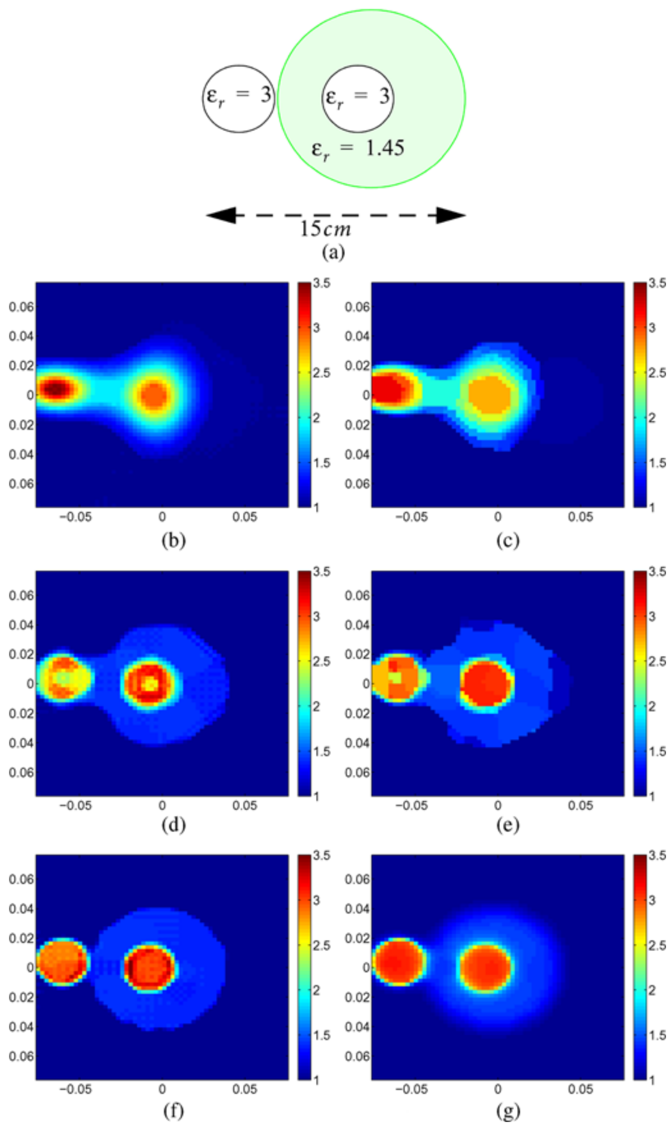

Fig. 3. Reconstruction of Fresnel data set *FoamTwinDiel*. DBIM with MR and the Laplacian regularizer reconstructions are on the left, and MR-CSI reconstructions are on the right. (a) Schematic of the scattering cylinders; (b),(c) reconstructions at 2 GHz; (d),(e) reconstructions at 6 GHz; (f),(g) full-frequency reconstructions 2–10 GHz.

transmitters, and 33 active receivers for each transmitter (64 total receiver positions). The data were collected at a frequency of 2.33 GHz. The data collection tank was filled with a background solution of water, with permittivity $\epsilon_b = 77.3 - j8.66$ at 2.33 GHz. We consider two different data sets: a biomedical phantom, FANTCENT and a real human forearm, BRAGREG. In all inversions in this section, the inversion results were restricted to lie within $0 \leq Re(\epsilon_r) \leq 80$ and $-20 \leq Im(\epsilon_r) \leq 0$ after each iteration, as the targets do not have permittivities higher than water.

1) Data Set FANTCENT: We utilize this data set to display the results from all different types of regularization for both the (MR)-CSI and DBIM algorithms. The FANTCENT set consists of a water and ethyl-alcohol based phantom. The schematic of the phantom, with the constituent materials and their permittivities is shown in Fig. 6(a). The reconstructions for the CSI

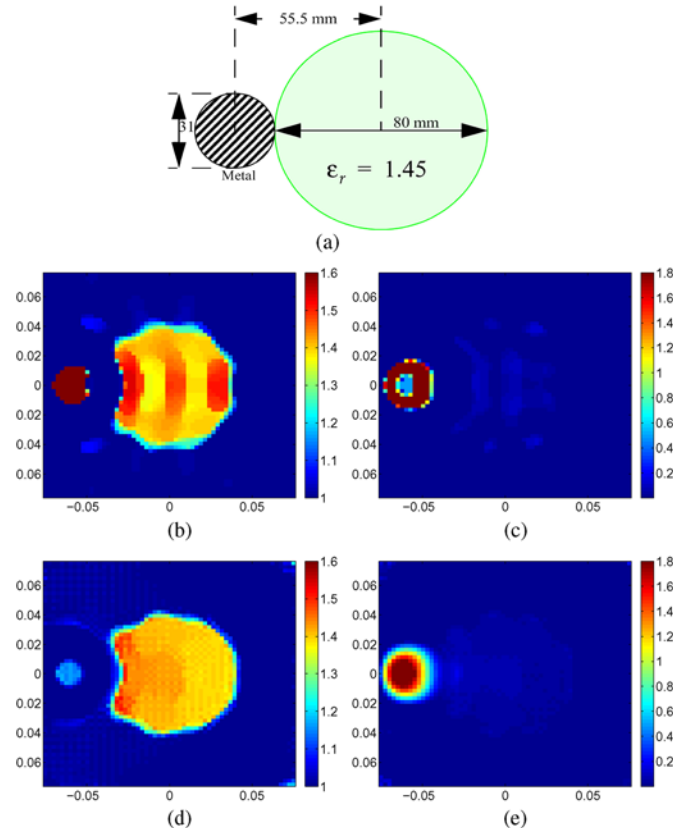

Fig. 4. Single frequency reconstructions of Fresnel Data set FoamMetExt. (a) Schematic of the scattering cylinders; (b),(c) MR-CSI reconstruction at 6 GHz; (d),(e) DBIM reconstructions at 6 GHz.

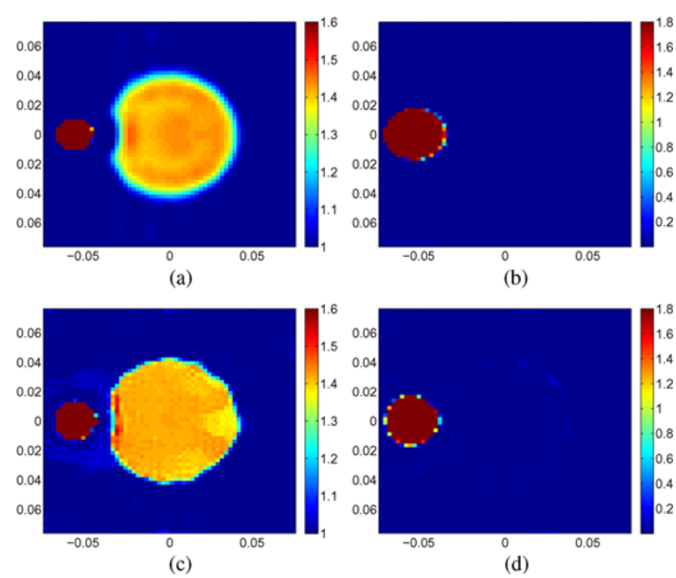

Fig. 5. Full-frequency reconstruction of Fresnel data set *FoamMetExt*. (a),(b) MR-CSI reconstructions from 2–18 GHz data; (b),(c) DBIM reconstructions from 2–18 GHz data. In this case, the differences between the images are primarily inside the copper rod, where no fields exist. In order to see the weakly scattering object, all images have been limited to a maximum pixel intensity.

and MR-CSI methods are shown in Fig. 7(a),(b) and (c),(d), respectively. The inversion results for the DBIM with the identity Tikhonov regularizer are shown in Fig. 7(e),(f), the results for DBIM with the Laplacian Tikhonov regularizer in Fig. 7(g),(h)

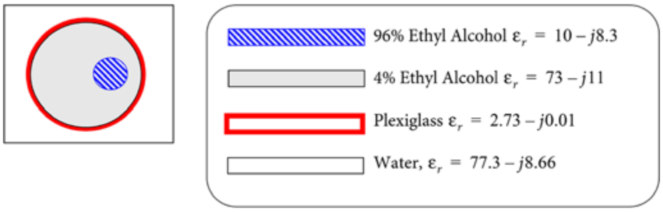

Fig. 6. The schematic of the 2D FANTCENT scatterer.

and the results for the DBIM with MR and the Laplacian regularizer are shown in Fig. 7(i),(j).

In this series of images, we can see the results of utilizing the different regularization schemes, and note the improvement in the both algorithms when MR is utilized. Qualitatively, the results for the CSI reconstruction lie somewhere between the DBIM-Identity and DBIM Laplacian results. However, we note that with the inclusion of the MR term that both methods provide qualitatively very similar, high quality, results [Fig. 7(c),(d) and (i),(j)].

It is hard to determine which inversion method provides the better result in this case. Both algorithms do not reconstruct the imaginary part of the permittivity very well, although there seems to be fewer oscillations in the MR-CSI reconstruction. However, the DBIM reconstruction obtains a closer result for the permittivity of the inner cylinder, particularly for the real part of the permittivity, where it reaches a value of $Re(\epsilon_r) = 15$, when the actual value should be $Re(\epsilon_r) = 10$. The MR-CSI algorithm reaches approximately $Re(\epsilon_r) = 20$.

We note here that two other groups [40], [41] were unable to blindly reconstruct this scatterer with the DBIM using Tikhonov regularization with the identity regularizer. We suspect that we were able to passably reconstruct this scatterer with the DBIM-identity algorithm due to the use of the L-curve to select the additive regularization parameter, which underlines the importance of regularization parameter selection.

2) Data Set BRAGREG: The final data set of the paper is the inversion of scattering data taken from a human forearm, or data set BRAGREG. The inversion results for the MR-CSI and DBIM are shown in Fig. 8. The expected relative permittivities at this frequency are approximately $\epsilon_r = 54 - j13$ for muscle, $\epsilon_r = 38.5 - j10$ for skin, $\epsilon_r = 8 - j1$ for bone marrow, and $\epsilon_r = 5.5 - j0.6$ for bone.

In this case it is difficult to determine which is a better reconstruction, due to the fact that there is no ideal case to compare the reconstructions with. In both cases, the overall structure of the arm may be seen in both the real and imaginary part of the reconstructions. The one advantage of the DBIM method is that it reaches closer to the expected value for the real part of the permittivity of the bones. However, we again note that the DBIM reconstruction with the identity regularizer (not shown) did not provide satisfactory results, emphasizing the importance of the Laplacian regularizer.

D. Computational Cost Evaluation

The computational costs of the two algorithms are outlined in Tables I and II, where the following conventions are used: the number of transmitters is given by T_x, the total number of

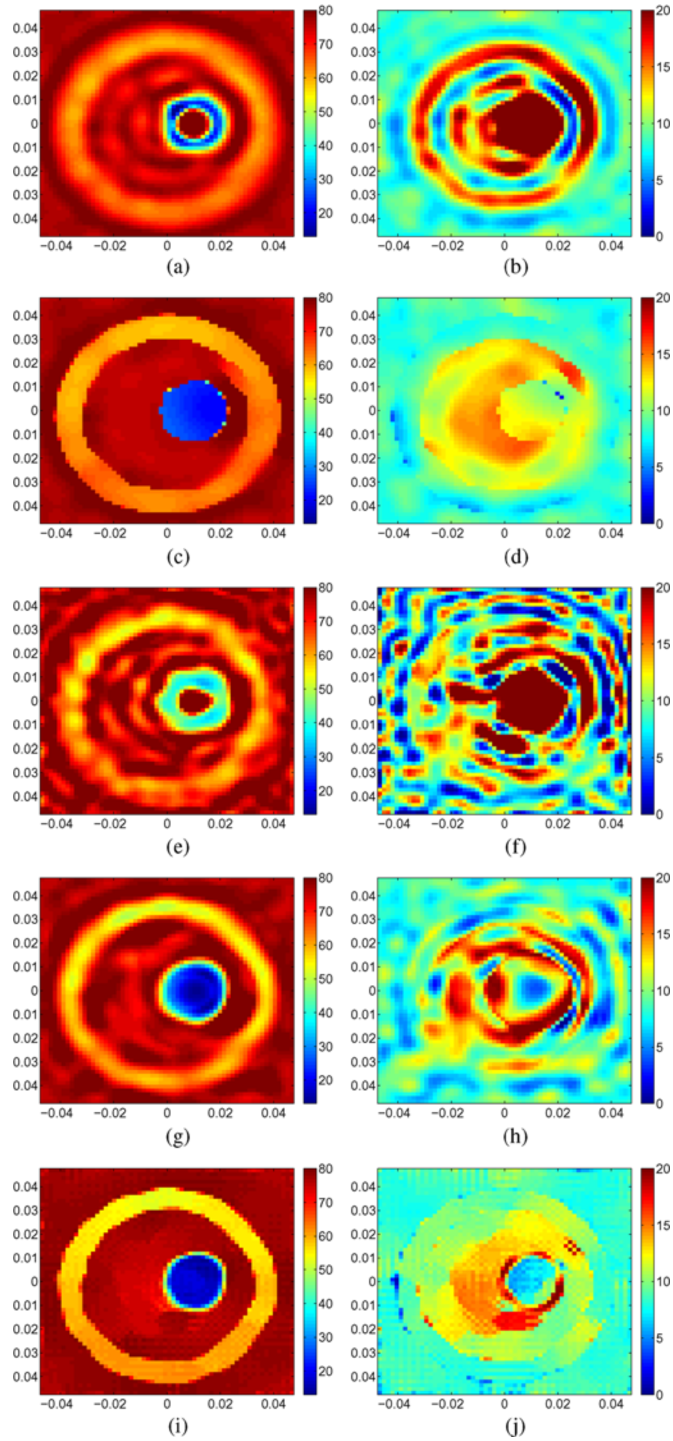

Fig. 7. Inversion of FANCENT data set: (a),(b) The inversion with the CSI method (no MR); (c),(d) the results of the MR-CSI method. (e),(f) The results for the DBIM with identity regularizer; (g),(h) DBIM with Laplacian; (i),(j) DBIM with MR and Laplacian regularizers. Qualitatively, (c),(d) and (i),(j) are quite similar.

unique receiver positions is represented by $R_x^{\rm tot}$, the number of active receivers for each transmitter is $R_x^{\rm act}$, the number of discretized elements in the mesh is given by N, and the number of steps in a Newton-type optimization, M_N. Each of these techniques also utilizes the conjugate-gradient (CG) algorithm (in the case of the DBIM, it is repeatedly utilized). In practice, the number of iterations required for the CG algorithm to

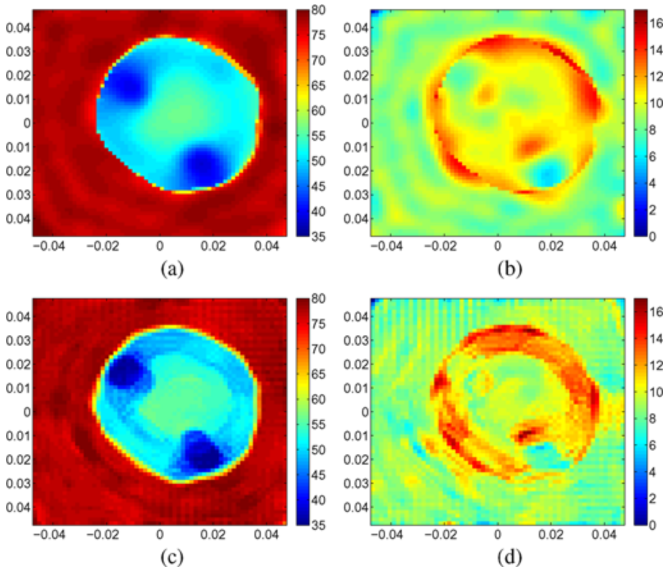

Fig. 8. Human forearm inversions: (a),(b) Results of the MR-CSI method. (c),(d) Results for the DBIM method with MR and Laplacian regularizer after 9 iterations.

TABLE I
COMPUTATIONAL COST OF MR-DBIM ALGORITHM

For each iteration of main MR-DBIM optimiation loop: M_N
  L-curve: $\propto 2M_{lbd}\left(T_x R_x^{\rm act} N + 2M_{cg}^{LP} N logN\right)$
  Tikhonov Parameter Solution: $\propto 2M_{cg}^{\rm Tikh}\left(T_x R_x^{\rm act} N + N logN\right)$
  For each transmitter: T_x
    call forward solver $\propto 2M_{cg}^{DB} N logN$
  end
  For total number of receivers: $R_x^{\rm tot}$
    call forward solver for distorted
    Green's function calc.: $\propto 2M_{cg}^{DB} N logN$
  end
end

TABLE II
COMPUTATIONAL COST OF MR-CSI ALGORITHM

For each iteration of main MR-CSI optimization loop: M_{cg}^{CSI}
  For each transmitter: T_x
    Data ($\mathcal{G}_{\rm S}$) Operators: $\propto 3R_x^{\rm act} N$
    Domain ($\mathcal{G}_{\rm D}$) Operators: $\propto 2N logN$
  end
end

converge varies widely depending on the particular problem. Thus, we introduce 4 different variables to be able to account for the different applications of the CG algorithm: we denote the number of iterations required for the main optimization loop in the CSI algorithm by $M_{cg}^{\rm CSI}$, the average number of iterations of the CG algorithm required to solve the Tikhonov functional (21) is denoted as M_{cg}^{Tikh}, the number of iterations required to solve the auxiliary system for the Laplacian regularizer (i.e., the system $z = R\delta\chi$) as $M_{cg}^{\rm LP}$, and the average number of iterations required for the Distorted-Born forward solver as $M_{cg}^{\rm DB}$. The number of Lanczos bidiagonalization algorithm iterations is denoted as M_{lbd}. For both DBIM and MR-CSI algorithms, we have ignored any operations which are proportional to N, which includes the MR operations for both algorithms.

Given the analysis in Tables I and II, the ratio of the DBIM to MR-CSI computational cost, υ, is given in (24)

$$\upsilon = \frac{2M_N}{M_{cg}^{\rm CSI}\left(3T_x R_x^{\rm act} + 2T_x logN\right)}\left(\left[M_{lbd} + M_{cg}^{Tikh}\right] T_x R_x^{\rm act} + \left[M_{cg}^{\rm DB}\{T_x + R_x^{\rm tot}\} + M_{cg}^{Tikh} + 2M_{cg}^{\rm LP} M_{lbd}\right] logN\right). \quad (24)$$

The exact value of this ratio υ will depend highly on the number of transmitters and receivers, as well as the exact conjugate gradient iteration numbers for each algorithm. The variations of the M parameters are both wide and problem dependent, which makes a generalized computational cost comparison very difficult. For example, the parameter $M_{cg}^{\rm DB}$ may vary from 10 to higher than 100, all on the same data set. We can, however, present the numbers we encountered for our data sets.

For example, in the FoamTwinDiel Fresnel data-set for the 2 GHz reconstruction, $N = 3600$, $T_x = 18$, and $R_x^{\rm tot} = 360$, $R_x^{\rm act} = 241$. The iteration numbers encountered were $M_N = 5$, $M_{cg}^{\rm DB} \approx 30$, $M_{cg}^{\rm LP} \approx 100$, $M_{lbd} \approx 30$, $M_{cg}^{Tikh} \approx 100$ and $M_{cg}^{\rm CSI} \approx 500$. Using these numbers, $\upsilon \approx 1.14$, and we thus expect the MR-CSI method to be slightly more efficient than the DBIM method. Our exact computation times were 29 minutes for the DBIM reconstruction, and 10 minutes for the MR-CSI reconstruction. However, we note that the DBIM was run as a highly optimized Matlab script running on quad core 2.66 GHz machine, while the CSI method was implemented in C++ and run as an executable on a single-core 1.73 GHz machine, so the exact computational times may be misleading.

As a second example, for the UPC Barcelona FANCENT data set, $T_x = 64$, $R_x^{\rm tot} = 64$, $R_x^{\rm act} = 33$ and $N = 3600$. The iteration-specific parameters were $M_N = 9$, $M_{cg}^{\rm DB} \approx 60$, $M_{cg}^{\rm LP} \approx 100$, $M_{lbd} \approx 30$, $M_{cg}^{Tikh} \approx 110$ and $M_{cg}^{\rm CSI} \approx 600$. In this case, the computational ratio comes out to $\upsilon \approx 1.75$, and we thus expect the MR-CSI method to be faster than the DBIM. Our exact computation times for these two data sets were 50 minutes for the DBIM and 16 minutes for the MR-CSI method. While some differences in the computational burden of these two algorithms exist, they are roughly on the same order of computational complexity. However, the CSI method holds an edge for all the cases we tested herein, and the fact that DBIM is at all competitive is based on utilizing well optimized stopping criteria for the multiple CG loops in the DBIM algorithm. While the selection of these stopping criteria is still done "blindly" if the number of iterations in each CG algorithm are allowed to increase even a small amount, the DBIM is much less efficient. We note that several methods of reducing computation time in the DBIM are available, such as adding a "marching-on-in-source-position" technique [38], which may decrease the average number of forward solver iterations, $M_{cg}^{\rm DB}$, low enough that the DBIM is competitive with the MR-CSI. Additionally, in the case where the positions of the transmitters and receivers are the same, as in the FANCENT test case, we note that the DBIM inversion may be made significantly more efficient. This can be accomplished because the computation of the distorted Greens function, (the loop over $R_x^{\rm tot}$ in Table I) may be eliminated, as the forward solver results in for the transmitter cases provide the identical results. However, these optimizations are problem dependent, and hard to predict in the general case.

VI. Discussion and Conclusion

Using an example of each of the two major classes of nonlinear inversion techniques, the MR-CSI and DBIM methods, we have blindly inverted a wide-range of data sets: noisy synthetic data, free-space far field data, and near-field water-submerged data. In these cases, the inversion results are remarkably similar. The exact computational burden for each algorithm is data-set dependent, but the MR-CSI method holds an advantage for computation time.

While the final images of the two algorithms are very similar, we note that the DBIM has many parameters which require the user to select before the inversion process begins: the accuracy of the Tikhonov solution, the accuracy of the Lanczos bidiagonalization to find the corner of the L-curve, the desired accuracy of the forward solver, the accuracy solution for the auxiliary system for the Laplacian regularizer, as well as the stopping condition for the main optimization loop. The particular selection of these parameters has significant impacts on the computational cost of the DBIM algorithm. For the MR-CSI method, the user only needs to select the stopping condition for the main optimization loop.

We also note that, from our experience, if the main optimization loop stopping condition of the DBIM is not selected appropriately, the algorithm may converge below the noise level in the data, and in this case provides oscillatory results. The MR-CSI method does not suffer from this problem, and remains stable even if the stopping condition is set well below the noise level.

The use of both (i) the Laplacian regularizer (instead of the identity regularizer), and (ii) MR in the DBIM were very important in the success of DBIM. While these modifications do add complications to the implementation of the algorithm, without either of these regularization changes the DBIM provided results which were not competitive with the MR-CSI algorithm. This can be seen in the FANTCENT example (Fig. 7). We note that if researchers have extant inversion codes which rely on the DBIM with the identity regularizer, it is relatively simple to add the Laplacian regularizer and MR to the algorithm, and this should provide results which are qualitatively very similar to the MR-CSI algorithm.

As can be seen from the results shown in this paper, the primary differences between these two inversion methods for TM data lie not in the inversion results, but in the implementation and computational complexity. In both of these metrics, MR-CSI is better than the DBIM, particularly in the ease of implementation.

Acknowledgment

The authors would like to thank the anonymous reviewers for suggesting the utilization of MR with the DBIM method as well as other important comments. They also acknowledge the support of NSERC, MITACS and Dr. S. Pistorius at CancerCare Manitoba. Thanks are also extended to J. Mallorqui for the UPC Barcelona Data set, and J.M. Geffrin, P. Sabouroux, and C. Eyraud for offering the Fresnel Data sets to the inverse problems community.

References

[1] S. Semenov, A. Bulyshev, A. Abubakar, V. Posukh, Y. Sizov, A. Souvorov, P. van den Berg, and T. Williams, “Microwave-tomographic imaging of the high dielectric-contrast objects using different image-reconstruction approaches,” *IEEE Trans. Microw. Theory Tech.*, vol. 53, no. 7, pp. 2284–2294, Jul. 2005.

[2] S. Y. Semenov, R. H. Svenson, V. G. Posukh, A. G. Nazarov, Y. E. Sizov, A. E. Bulyshev, A. E. Souvorov, W. Chen, J. Kasell, and G. P. Tastis, “Dielectrical spectroscopy of canine myocardium during acute ischemia and hypoxia at frequency spectrum from 100 khz to 6 ghz,” *IEEE Trans. Med. Imag*, vol. 21, no. 6, pp. 703–707, June 2002.

[3] T. Rubaek, P. M. Meaney, P. Meincke, and K. D. Paulsen, “Nonlinear microwave imaging for breast-cancer screening using Gauss-Newton’s method and the CGLS inversion algorithm,” *IEEE Trans. Antennas Propag.*, vol. 55, no. 8, pp. 2320–2331, Aug. 2007.

[4] J. M. Sill and E. C. Fear, “Tissue sensing adaptive radar for breast cancer detection-experimental investigation of simple tumor models,” *IEEE Trans. Microw. Theory Tech.*, vol. 53, no. 11, pp. 3312–3319, Nov. 2005.

[5] E. C. Fear, X. Li, S. C. Hagness, and M. Stuchly, “Confocal microwave imaging for breast cancer detection: Localization of tumors in three dimensions,” *IEEE Trans. Biomed Eng.*, vol. 49, no. 8, pp. 812–822, Aug. 2002.

[6] E. Bond, X. Li, S. C. Hagness, and B. D. van Veen, “Microwave imaging via space-time beamforming for early detection of breast cancer,” *IEEE Trans. Antennas Propag.*, vol. 51, no. 8, pp. 1690–1705, Aug. 2003.

[7] P. Kosmas and C. M. Rappaport, “FDTD-based time reversal for microwave breast cancer detection-localization in three dimensions,” *IEEE Trans. Microw. Theory Tech.*, vol. 54, no. 4, pp. 1921–1927, Jun. 2006.

[8] R. K. D. Colton, *Inverse Acoustic and Electromagnetic Scattering Theory*. Berlin: Springer-Verlag, 1998.

[9] J. D. Zaeytijd, A. Franchois, C. Eyraud, and J. Geffrin, “Full-wave three-dimensional microwave imaging with a regularized Gauss-Newton method-theory and experiment,” *IEEE Trans. Antennas Propag.*, vol. 55, no. 11, pp. 3279–3292, Nov. 2007.

[10] W. C. Chew and Y. M. Wang, “Reconstruction of two-dimensional permittivity distribution using the distorted born iterative method,” *IEEE Trans. Med. Imaging*, vol. 9, no. 2, pp. 218–225, 1990.

[11] S. Caorsi, A. Massa, and M. A. Pastorino, “A computational technique based on a real-coded genetic algorithm for microwave imaging purposes,” *IEEE Trans. Geosci. Remote Sensing*, vol. 38, no. 4, pp. 1697–1708, 2000.

[12] R. E. Kleinman and P. M. van den Berg, “A modified gradient method for two-dimensional problem in tomography,” *J. Comput. Appl. Math.*, vol. 42, no. 1, pp. 17–35, 1992.

[13] P. M. van den Berg and R. E. Kleinman, “A contrast source inversion method,” *Inverse Probl.*, vol. 13, pp. 1607–1620, 1997.

[14] A. Abubakar, P. M. van den Berg, and J. J. Mallorqui, “Imaging of biomedical data using a multiplicative regularized contrast source inversion method,” *IEEE Trans. Microw. Theory Tech.*, vol. 50, no. 7, pp. 1761–1777, Jul. 2002.

[15] A. Abubakar and P. M. van den Berg, “Iterative forward and inverse algorithms based on domain integral equations for three-dimensional electric and magnetic objects,” *J. Comput. Phys.*, vol. 195, pp. 236–262, 2004.

[16] A. Abubakar, P. M. van den Berg, and S. Y. Semenov, “Two- and three-dimensional algorithms for microwave imaging and inverse scattering,” *J. Electromagn. Waves. Applicat.*, vol. 17, no. 2, pp. 209–231, 2003.

[17] A. Abubakar, T. M. Habashy, V. L. Druskin, L. Knizhnerman, and D. Alumbaugh, “2.5D forward and inverse modeling for interpreting low-frequency electromagnetic measurements,” *Geophysics*, vol. 73, no. 4, pp. F165–F177, Jul.-Aug. 2008.

[18] V. A. Morozov, *Methods for Solving Incorrectly Posed Problems*. New York: Springer, 1984.

[19] P. C. H. D. Calvetti and L. Reichel, “L-curve curvature bounds via Lanczos bi-diagonalization,” *SIAM J. Scientific Comput.*, vol. 14, pp. 20–25, 2002.

[20] P. C. Hansen and D. P. O’Leary, “The use of the L-curve in the regularization of discrete ill-posed problems,” *SIAM J. Scientific Comput.*, vol. 14, pp. 1487–1503, 1993.

[21] A. Abubakar and P. M. van den Berg, “Total variation as a multiplicative constraint for solving inverse problems,” *IEEE Trans. Image Process.*, vol. 10, no. 9, pp. 1384–1392, Sep. 2001.

[22] R. F. Bloemenkamp, A. Abubakar, and P. M. van den Berg, “Inversion of experimental multi-frequency data using the contrast source inversion method,” *Inverse Probl.*, vol. 17, pp. 1611–1622, 2001.
[23] A. Abubakar, P. M. van den Berg, and T. M. Habashy, “Application of the multiplicative regularized contrast source inversion method on TM- and TE-polarized experimental Fresnel data,” *Inverse Probl.*, vol. 21, pp. S5–S13, 2005.
[24] P. Zwamborn and P. van den Berg, “The three dimensional weak form of the conjugate gradient FFT method for solving scattering problems,” *IEEE Trans. Microw. Theory Tech.*, vol. 40, no. 9, pp. 1757–1766, Sep. 1992.
[25] R. F. Remis and P. M. van den Berg, “On the equivalence of the Newton-Kantorovich and distorted Born methods,” *Inverse Problems*, vol. 16, pp. L1–L4, 2000.
[26] E. Chong and S. Zak, *An Introduction to Optimization*. New York: Wiley Interscience, 2001.
[27] T. J. Connolly and D. J. Wall, “On the Frechet differentialbility of some nonlinear operators occurring in inverse problems: An implicit function theorem approach,” *Inverse Problems*, vol. 6, pp. 949–966, 1990.
[28] P. C. Hansen, “Numerical tools for analysis and solution of Fredholm integral equations of the first kind,” *Inverse Problems*, vol. 8, pp. 849–872, 1992.
[29] A. N. Tikhonov, “Regularization of incorrectly posed problems,” *Soviet Math Dokl.*, vol. 4, pp. 1624–1627, 1963.
[30] T. K. Jensen, “Stabilization algorithms for large-scale problems,” Ph.D. dissertation, Technical Univ. Denmark, Kongens Lyngby, Denmark, 2006.
[31] G. H. Golub, M. Heath, and G. Wahba, “Generalized cross validation as a method for choosing a good ridge parameter,” *Technometrics*, vol. 21, pp. 215–224, 1979.
[32] M. E. K. P. C. Hansen and R. H. Kjeldsen, “Exploiting residual information in the parameter choice for discrete ill-posed problems,” *BIT Numerical Math.*, vol. 46, pp. 41–59, 2006.
[33] P. Mojabi and J. LoVetri, “Preliminary investigation of the NCP parameter choice method for inverse scattering problems using BIM: 2-D TM case,” *ACES J.*, vol. 23, no. 3, pp. 207–214, Sep. 2008.
[34] A. Abubakar, P. M. van den Berg, T. M. Habashy, and H. Braunisch, “A multiplicative regularization approach for deblurring problems,” *IEEE Trans. Image Process.*, vol. 13, no. 11, pp. 1524–1532, Nov. 2004.
[35] J. Richmond, “Scattering by a dielectric cylinder of arbitrary cross section shape,” *IEEE Trans. Antennas Propag.*, vol. 13, pp. 334–341, May 1965.
[36] S. G. C. Gabriel and E. Corthout, “The dielectric properties of biological tissues: III. parametric models for the dielectric spectrum of tissues,” *Phys. Med. Bio.*, vol. 41, no. 11, pp. 2271–2294, 1996.
[37] J.-M. Geffrin, P. Sabouroux, and C. Eyraud, “Free space experimental scattering database continuation: Experimental set-up and measurement precision,” *Inverse Probl.*, vol. 21, pp. S117–S130, 2005.
[38] Z. Peng and A. G. Tijhuis, “Transient scattering by a lossy dielectric cylinder: Marching-on-in-frequency approach,” *J. Electromag. Waves Applicat.*, vol. 7, pp. 739–763, 1993.
[39] J. C. B. J. J. Mallorqui, N. Joachimowicz, and A. P. Broquetas, “Database of ‘in-vivo’ measurements for quantitative microwave imaging and reconstruction algorithms available,” *IEEE Antennas Propag. Mag.*, vol. 37, no. 5, pp. 87–89, 1995.
[40] N. Joachimowicz, J. J. Mallorqui, J. C. Bolomey, and A. Broquetas, “Convergence and stability assessment of Newton-Kantorovich reconstruction algorithms for microwave tomography,” *IEEE Trans. Med. Imag.*, vol. 17, pp. 562–569, Aug 1998.
[41] W. C. Chew and J. H. Lin, “A frequency-hopping approach for microwave imaging of large inhomogeneous bodies,” *IEEE Microw. Guided Wave Lett.*, vol. 5, no. 12, pp. 439–441, Dec. 1995.

Colin Gilmore (S’05) received the B.Sc. and the M.Sc. degrees in electrical engineering from the University of Manitoba, Winnipeg, MB, Canada, in 2002 and 2005, respectively, where he is currently working toward the Ph.D. degree.

During 2008, he completed an internship at Schlumberger-Doll Research, Cambridge, MA. His current research interests are in the areas of electromagnetic inversion, computational electromagnetics and inverse problems.

Mr. Gilmore was awarded a Canadian Natural Sciences and Engineering Research Council (NSERC) Postgraduate Scholarship A from 2002 to 2004, an NSERC Canada Graduate Scholarship from 2005 to 2008, and currently holds a Manitoba Health Research Council Scholarship.

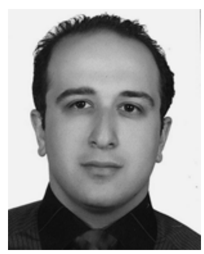

Puyan Mojabi received the B.Sc. degree in electrical and computer engineering from the University of Tehran, Tehran, Iran, in 2002 and the M.Sc. degree in electrical engineering from Iran University of Science and Technology, in 2004. Currently, he is working toward the Ph.D. degree at the University of Manitoba, Winnipeg, MB, Canada.

His current research interests are computational electromagnetics and inverse problems.

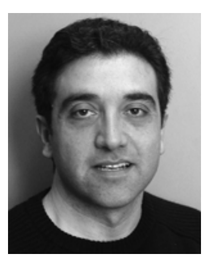

Joe LoVetri (SM’09) received the Ph.D. degree in electrical engineering from the University of Ottawa, ON, Canada, in 1991.

From 1991 to 1999, he was an Associate Professor in the Department of Electrical and Computer Engineering, University of Western Ontario, Canada. He is currently a Professor in the Department of Electrical and Computer Engineering and Associate Dean (Research) of the Faculty of Engineering at University of Manitoba, Winnipeg, Canada. His main research interests are in time-domain CEM, modeling of EMC problems, GPR, and inverse imaging techniques.